WILEY

The Institution of
Engineering and Technology

ORIGINAL RESEARCH OPEN ACCESS

Forced Air-Cooling of Modular Flux Switching PM Machines Using Flux Gaps as Cooling Channels

Guan-Bo Zhang | Guang-Jin Li

School of Electrical and Electronic Engineering, The University of Sheffield, Sheffield, UK

Correspondence: Guang-Jin Li (g.li@sheffield.ac.uk)

ABSTRACT

This paper investigates the thermal performance of modular flux-switching permanent magnet (FSPM) machines under forced air cooling. Unlike conventional designs with continuous stator iron core, the modular configuration with segmented stator core introduces flux gaps between stator segments that can be used as extra cooling channels to increase the internal heat exchange surface area. To assess the impact of this innovative cooling design, models with varying flux gap widths (0–8 mm) were analysed using 3D computational fluid dynamics (CFD) modelling. Results indicate that at constant inlet air speed, the lowest machine temperature is achieved at 1 mm flux gap. Under constant pressure loss, the optimal cooling is achieved at a 4 mm flux gap. Although extreme flux gap widths hinder the cooling efficiency, the modular FSPM machines still outperform their nonmodular counterparts thermally. The study also examines the effect of rotor speed, revealing that higher speeds induce greater turbulence and reduce machine temperature, particularly beyond 2800 rpm, albeit with increased system pressure loss. The CFD simulation results were validated through a series of thermal experiments, confirming the accuracy of the CFD models and demonstrating the feasibility of using flux gaps as cooling channels in modular FSPM machines.

1 | Introduction

Permanent magnet (PM) machines are widely used in industrial applications, and the demand for high power density and high-speed PM machines is growing, particularly in areas such as electric vehicles, wind turbines and aerospace systems. However, high power density and high-speed operation result in significantly increased power losses within the machine, especially in the coils and magnets, which are particularly susceptible to high temperatures. Elevated temperatures can lead to magnet demagnetisation, insulation breakdown and, ultimately, system failure. Therefore, effective thermal management is becoming increasingly critical in the electrical design of PM machines.

Forced air cooling is an important cooling method for electrical machines. It is established that the forced air cooling is suitable for machines with current density at 5–10 A/mm^2 [1]. Although as the current density increases, using air as the coolant is not enough and forced liquid cooling should be adopted; forced air cooling is still preferred for low to medium power electrical machines due to its simplicity, lower cost and ease of implementation and maintenance [2]. The forced air cooling can be classified into total enclosed fan-cooled (TEFC) and open fan cooled (OFC) machines depending on the air flow route [3].

In a TEFC machine, an external fan—typically mounted on the rotor shaft—blows air over the machine housing, which is completely enclosed. The airflow passes across the housing

surface, and external fins can be added to increase the effective heat transfer surface area [4]. In such systems, the cooling performance depends on several factors, including the type of fan (centrifugal or axial) [5], the number of fan blades [6], the blade shape [7] and even the fan's rotational direction [8]. However, heat transfer in the end-winding space remains limited due to the confined air between the machine components and the housing. To enhance heat dissipation in this region, internal fans mounted on the shaft or wafters mounted on the rotor lateral surface can improve air circulation, allowing heat from the end-windings to be transferred to the housing through internal airflow [9]. Once such inner circulation is established, estimating the end-space convection coefficient becomes critical. Both computational fluid dynamics (CFD) simulations and experimental measurements have been employed to study the relationship between rotor speed and convection coefficients [10, 11]. Further studies also investigate the cooling performance and friction losses introduced by wafters [12]. Although the enclosed frame inherently limits cooling capability, it provides significant advantages by preventing dust ingress and reducing acoustic noise [13].

In an OFC machine, cooling performance is significantly enhanced, as cold air from the ambient environment is continuously drawn into the machine and allowed to directly contact the internal components such as end-windings and PMs. Traditionally, the external fan is either mounted on the shaft or driven independently by an air pump. The cooling capability of a shaft-mounted fan is constrained by the machine's operating speed and introduces additional windage losses, making it unsuitable for medium and large motors [14]. By contrast, an independent fan (air pump) provides constant airflow regardless of machine speed and offers greater flexibility in flow channel design. However, the number, position and area of air inlets are critical to thermal performance [15–17], and this approach requires an additional power supply and control system, which increases overall complexity. Beyond traditional fan configurations, certain electrical machines with salient rotors can be designed so that the rotor itself functions as a fan. For example, the authors in ref. [18]

report on a novel flux-switching permanent magnet (FSPM) machine with a rotor shaped-like fan blades. This design enables the machine to operate simultaneously as a motor and as an axial fan, thereby cooling itself.

The modular flux-switching permanent magnet (FSPM) machine [19], as a stator-mounted PM configuration [20] shown in Figure 1, places both coils and magnets on the stationary stator, where more effective cooling strategies can be applied compared to rotor-mounted PM designs. Moreover, the modular FSPM machine is expected to demonstrate superior thermal performance relative to conventional FSPM machines, owing to the additional heat exchange surface area provided by the flux gap region. Although positioning the magnets closer to the ambient environment offers certain thermal benefits, it also places them in proximity to the windings, which is the primary heat source of the machine. Consequently, studies have shown that magnet temperatures tend to closely follow those of the windings, with both rising in tandem [21].

Nevertheless, the modular design and the presence of a flux gap provide clear advantages when a forced cooling system is employed [22–25]. Although previous studies have demonstrated that the flux gaps can effectively lower the temperature of PM machines, most of this research has concentrated on modular surface-mounted PM (SPM) machines in which the PMs are mounted on the rotor outer surface. In contrast, the impact of forced air cooling on modular FSPM machines has not yet been thoroughly explored. In particular, the FSPM machines feature a salient rotor design, which can significantly influence internal airflow and, consequently, the cooling efficiency of the flux gaps in modular FSPM machines.

In this paper, a forced air-cooling system is implemented for a 12-slot/14-pole modular FSPM machine, whose electromagnetic performance is enhanced by the introduction of flux gaps. To analyse the factors influencing thermal performance, a series of 3D CFD models with varying flux gap widths (from 0 to 8 mm) have been developed. Additionally, the rotation of the salient rotor induces significant turbulent airflow in both the air gap
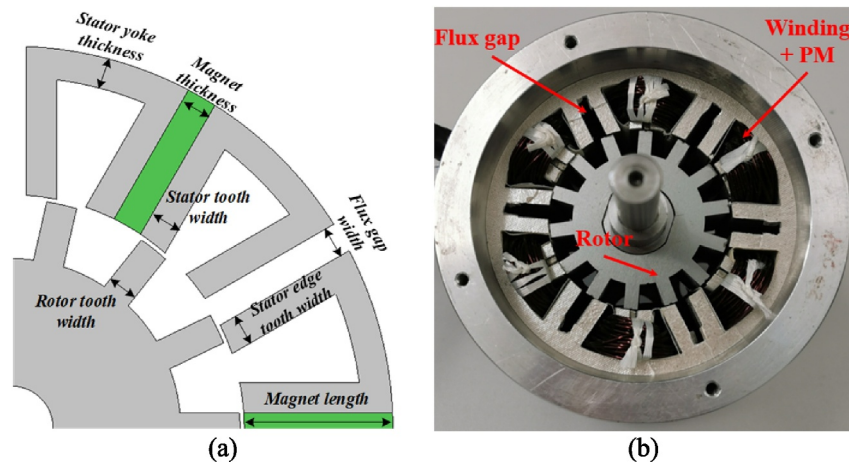

FIGURE 1 | A 12-slot/14-pole modular FSPM machine studied in this paper. (a) Cross-sectional view and (b) prototype machine for experimental validation.

and the flux gap regions. Therefore, the impact of rotor speed on thermal performance is also explored in this paper.

2 | Machine Specifications and Detailed CFD Modelling

2.1 | Machine Specifications

In ref. [26], a 12-slot/14-pole modular FSPM machine has been optimised using a multi-objective genetic algorithm. The machine selected for the analyses in this paper is derived from the optimised results. The specifications of this machine are listed in Table 1 and the cross-section is illustrated in Figure 1. It is worth noting that to obtain a nonmodular FSPM machine, one can reduce the flux gap width to 0 mm, leading to an E-core structure. In this process, the iron section of the teeth is unchanged, but the slot area can be increased accordingly.

2.2 | CFD Modelling

CFD modelling is gaining increasing popularity for the thermal analysis of electrical machines, especially those with forced air or liquid cooling, where convection coefficients cannot be easily obtained from empirical equations. In the CFD modelling, the fluid motion is primarily governed by the conservation equations of mass, momentum and energy, which will be discussed briefly in the following sections.

2.2.1 | Governing Equations

The conservation of mass equation states that the rate of change of mass within a fluid element is equal to the net mass flow into the element. This principle is commonly known as the continuity equation [27] as described by

$$\frac{\partial \rho}{\partial t} + \nabla \cdot (\rho V) = 0 \tag{1}$$

where ρ is the fluid density, t is the time and V is the velocity vector.

The conservation of momentum equation states that the rate of change of a fluid particle's momentum is equal to the sum of the forces acting on the fluid element. Based on Newton's second law, this equation is commonly known as the Navier–Stokes equation [27]:

$$\rho \left(\frac{\partial V}{\partial t} + V \cdot \nabla V \right) = -\nabla p + \nabla \tau_{ij} + pg \tag{2}$$

where ∇p is the pressure force component, $\nabla \tau_{ij}$ is the viscous force component, which is due to viscous stress, and pg is the gravitational force component. The left side term is the local acceleration and convective acceleration, which originates from the term dV/dt, that is, the fluid particle acceleration. It is stated that the pg term is negligible when the working fluid is gas for forced convection cases [28].

The conservation of energy equation states that the rate of change of a fluid particle's energy is equal to the sum of the net heat added to the particle and the net work done on it. This equation is based on the first law of thermodynamics [27] such as

$$\frac{\partial T}{\partial t} + V \cdot \nabla T = \alpha \nabla^2 T + \Phi \tag{3}$$

where $\frac{\partial T}{\partial t}$ is the local (time) rate of change of temperature T, $(V \cdot \nabla T)$ is the convective transport of heat due to a velocity field which represents how heat moves with the flow of a fluid, $\alpha \nabla^2 T$ is the diffusive term, $\alpha = k/(\rho c_p)$ is the thermal diffusivity, k is thermal conductivity, ρ is density, c_p is specific heat at constant pressure and Φ is a source term representing internal heat generation.

2.2.2 | Turbulence Model and Rotation Model

The governing equations discussed above can be used to solve laminar flow problems. However, turbulent flow in rotating electrical machines requires the Reynolds-Averaged Navier–Stokes (RANS) approach. In this method, turbulent flow variables are decomposed into time-averaged and fluctuating components, providing sufficient accuracy to quantify turbulent flow characteristics. As a result, the RANS approach is widely used in the thermal analysis of electrical machines. The k-ε and k-ω models are the most commonly used two-equation turbulence models in the RANS approach, where k represents turbulent kinetic energy, ε denotes the turbulence dissipation rate and ω is the specific turbulence dissipation rate [13]. In this paper, the Shear Stress Transport (SST) k-ω model is adopted. This model is well-known for its suitability in capturing swirling flows without

TABLE 1 | Parameters of modular FSPM machine.

Slot number	12	Air gap length (mm)	0.5
Pole number	14	Stack length (mm)	25
Stator outer radius (mm)	45	Stator yoke thickness (mm)	4.1
Stator inner radius (mm)	26.6	Stator edge tooth width (mm)	3.8
Magnet thickness (mm)	2.7	Stator tooth width (mm)	3.3
Flux gap width (mm)	4	Rotor tooth width (mm)	4.1
Rate speed (rpm)	400	Housing length (mm)	70

requiring sublayer damping while also improving separation flow prediction.

Rotor rotation also plays a crucial role in determining the flow field and pressure distribution in electrical machines. The main method for modelling rotational effects is the moving reference frame (MRF) which is also known as the frozen rotor approach. It is adopted in this paper for the steady-state analysis of the rotating machines. In the MRF approach, the rotational region does not physically move. However, the effects of rotation, such as Coriolis and centrifugal forces, are accounted for. The main drawback of this method is that, since the rotor remains fixed relative to the stator, different relative positions can lead to varying results [28].

2.2.3 | Heat Transfer Coefficient

The heat transfer coefficient is a crucial parameter for analysing heat transfer in electrical machines. According to the ANSYS CFX modelling guide [29], the heat transfer coefficient is calculated by

$$q_w = h_c(T_w - T_{nw}) \tag{4}$$

where q_w is the heat flux across the wall boundary, T_w is the wall temperature, T_{nw} is the near-wall temperature and h_c is the heat transfer coefficient. The near-wall temperature T_{nw} represents the fluid temperature at the first fluid node adjacent to the wall. However, when calculating the heat transfer coefficient h_c using the near-wall temperature T_{nw}, the result is highly dependent on the mesh resolution. With a fine mesh, the near-wall temperature approaches the wall temperature, causing the denominator in Equation (4) to approach zero, which results in extremely large values for h_c. Another approach that can be used in CFX is to change the 'T_{bulk} for HTC' of 'expert parameter' in the CFX-pre. The heat transfer coefficient will be calculated by [29]

$$h_c = \frac{q_w}{(T_w - T_{bulk})} \tag{5}$$

where T_{bulk} represents the average temperature of the fluid in the vicinity of a wall.

2.2.4 | Thermal Modelling and Conditions

In the forced air-cooled modular FSPM machine, six inlets and outlets, each with a radius of 10 mm, are incorporated into the machine housing. These inlets and outlets are positioned to face the end-windings, as the authors in ref. [22] have shown that this design is more effective in reducing winding temperatures. Due to the periodic nature of the 12-slot/14-pole machine's stator and rotor, they can be represented using a periodic sector. As a result, one-sixth of the stator and one-fourteenth of the rotor are simulated using ANSYS CFX software. The CFD model is divided into a stationary region and a rotating region, connected by an automatic pitch change interface, as illustrated in Figure 2. According to the CFX theory guide [29], for frame change interfaces, the interface internally accounts for pitch
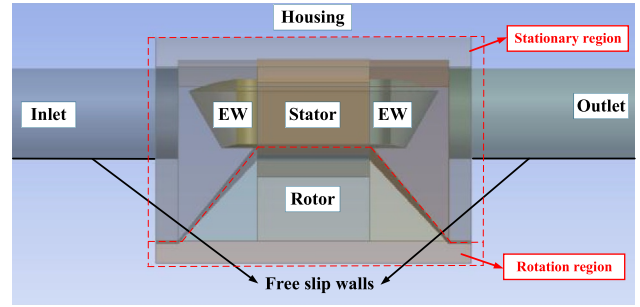

FIGURE 2 | CFD model of the modular FSPM machine with forced air cooling.

variations by scaling the local flows up or down as they cross the interface.

To prevent unwanted backflow, the upstream and downstream regions are designed with lengths approximately 2 times of the machine length. Additionally, the walls of these regions are set as free-slip boundaries to ensure that airflow entering or exiting the machine is not affected by wall shear stress. In the simulations, air is treated as an incompressible fluid, as airflow in electrical machines typically remains below 0.3 Mach. However, air compressibility becomes significant when the velocity exceeds 100 m/s in electrical machines [27]. The property of the air is as follows: density is 1.185 kg/m³, thermal conductivity is 0.0261 W/m·K, dynamic viscosity is 1.831×10^{-5} Pa·s and specific heat capacity is 1004.4 J/kg·K.

The thermal properties of both the machine components and air are consistent with the previous analysis. The convection coefficient of the housing surfaces is set to 15 W/m²·K, and the ambient temperature is maintained at 25°C. In the simulation, the winding region employs equivalent thermal conductivity values in different directions. These values, obtained from the ANSYS Motor-CAD software package, are 0.87 W/m·K in the circumferential and radial directions and 265 W/m·K in the axial direction. The essential thermal conductivities in W/m·K are 168 for the housing, 30 for stator and rotor core, 7.6 for magnet and 52 for shaft. The thermal contact resistance between the stator core and housing is represented by an equivalent air gap between the solid surfaces, with an adopted air gap length of 0.03 mm. In addition, the thermal model of bearings uses an equivalent interface gap of 0.3 mm [30].

2.2.5 | CFD Model Mesh

Finally, mesh quality in the CFD model is critical to ensuring accurate simulation results. For the mesh generation, both tetrahedron and six-sided hexahedron types of cells are utilised using ANSYS meshing software. The overall mesh size for the machine and its surrounding air region is set to 1 mm. In the air gap region, where highly turbulent airflow occurs, a finer mesh size of 0.2 mm is applied. Additionally, a five-layer inflation mesh with a first layer thickness of 0.028 mm is implemented on the air gap surfaces as well as flux gap surfaces attached to both the stator and rotor. For the other surfaces of the air region in contact with solid walls, a five-layer inflation mesh with a smooth transition is applied. It should be noted that for all
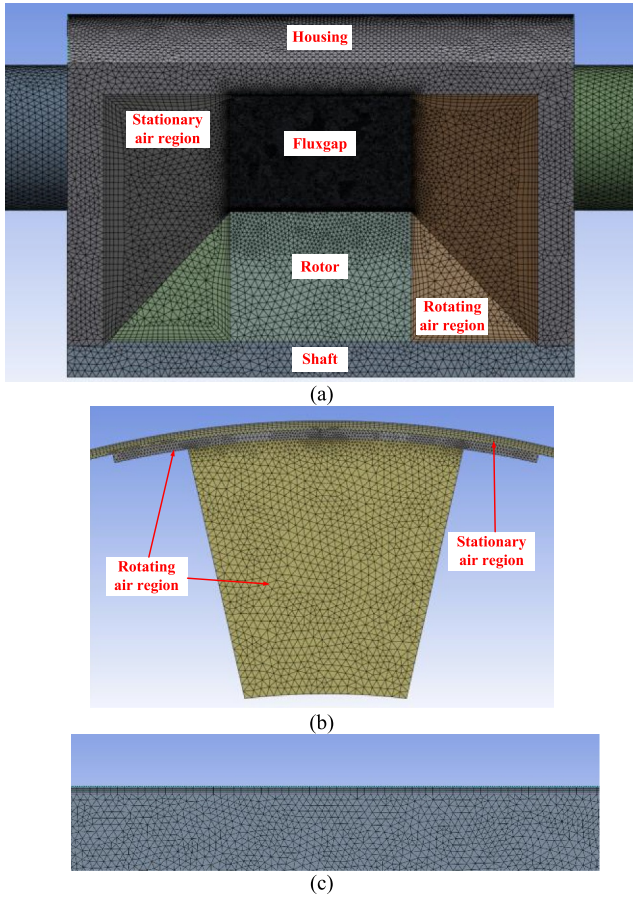
FIGURE 3 | (a) Meshes on the cross-section plane, (b) in the air gap region and (c) in the flux gap region of the investigated modular FSPM machine.

inflation meshes, the growth rate is 1.2. These meshes are shown in Figure 3. As a result, the generated mesh has 2,417,646 nodes and 11,584,798 elements. The simulations are conducted by a computer with 64 gigabyte RAM and an 8-core CPU Intel Xeon W-2245. The calculated time for each case is around 8 h.

3 | Results and Discussions

For the modular SPM machine investigated in refs. [24, 25], flux gaps serve as additional airflow channels and provide extra surface areas for heat dissipation, enhancing its thermal performance compared to conventional SPM machines. The width of the flux gap also plays a crucial role in cooling efficiency. If the flux gap is too narrow, airflow over the machine becomes restricted. Conversely, if the flux gap is too wide, the coolant velocity decreases significantly at the same inlet speed, reducing the cooling effectiveness.

The modular FSPM machine differs from the modular SPM machine in terms of airflow characteristics. In an SPM machine, if flux gaps are not introduced, the only available airflow path is the air gap, which is typically kept as narrow as possible to maximise electromagnetic performance. However, in an FSPM machine, even without flux gaps, the rotor's salient

structure naturally provides sufficient channels for airflow. As a result, the effectiveness of flux gaps in enhancing cooling performance might be reduced compared to their impact on SPM machines.

The original design of the modular FSPM machine features a 4-mm flux gap. To analyse the impact of flux gap width on thermal performance, several additional modular FSPM machine models are developed with flux gaps ranging from 0 to 8 mm. When the flux gap is reduced to 0 mm, the modular FSPM machine essentially becomes a nonmodular, E-core FSPM machine.

The thermal performance of an FSPM machine is strongly influenced by loss distribution, as both iron losses and PM eddy current losses increase significantly with rotor speed. To isolate the effects of inlet conditions and fluid behaviour within the machine, the copper loss is fixed at 150 W, and iron and PM eddy current losses are first neglected in Sections 3.3 and 3.5 so that the cooling effectiveness can be easily observed by winding temperature variations.

Furthermore, changes in the flux gap width affect the machine's coil resistance by modifying the slot area and end-winding length. The corresponding resistance values can be calculated using Equations (6) and (7) and provided in Table 2.

$$R = \frac{L}{\sigma \cdot F_{slot} \cdot \frac{S_{slot}}{N_{slot}}} \quad (6)$$

where σ is the copper conductivity ($5.95 \times 10^7/\Omega m$), L is the total conductor length including active winding and end-winding (L_{end}), S_{slot} is the single slot area, F_{slot} is the slot fill factor which is 0.3 and N_{slot} is the number of turns for a single slot. As for the length of a single coil, the active length is equal to the machine's stack length and the end winding length in this machine can be calculated by

$$L_{end} = \pi \cdot \left(W_{slot} + W_{stator} + \frac{1}{2} W_{PM} \right) \quad (7)$$

where W_{slot} is the average stator slot width, W_{stator} is the stator tooth width and W_{PM} is the thickness of the magnet. Table 2 lists the resistance of the modular FSPM machine at different flux gap widths.

Figure 4 shows the injected current and average torque at different flux gap widths under a constant copper loss of 150 W. As the flux gap widens, the slot area decreases, leading to an increase in machine resistance as shown in Table 2. To maintain the fixed copper loss, the injected current must be reduced. Despite this current reduction, the average torque peaks at a flux gap width of 5 mm. This is because, as noted in ref. [31], the flux gap can improve the winding factor in 12s/14p modular machines, thereby enhancing torque performance. Consequently, the positive effect of the improved winding factor outweighs the negative effect of the reduced current at this optimal point. However, beyond 5 mm, a wider flux gap causes the winding factor to decline while the current continues to decrease, which together aggravate the reduction in average torque.

TABLE 2 | Resistance of modular FSPM at different flux gap widths.

Flux gap (mm)	Coil length (mm)	Slot area (mm^2)	Resistance (Ω)
0	111.2	131.5	0.36
1	109.6	124.3	0.38
2	108.1	117.3	0.40
3	106.4	109.8	0.42
4	104.8	102.6	0.44
5	103.2	95.3	0.47
6	101.6	88.0	0.50
7	100.1	80.7	0.54
8	98.4	73.3	0.58
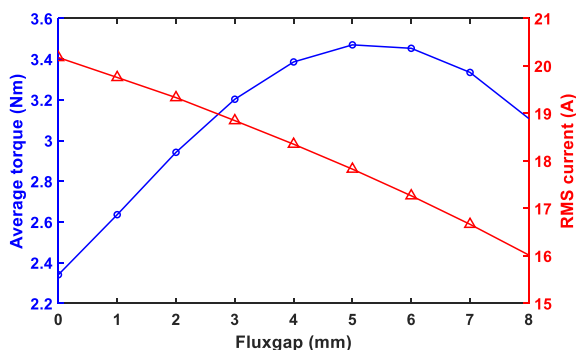
FIGURE 4 | Average torque and injected RMS current versus flux gap width (150 W).

3.1 | Comparison Between Natural and Forced Air Cooling

In order to show the advantages of forced air cooling with flux gaps, a comparison in terms of RMS current, torque, power and efficiency between the forced air cooled and natural air cooled 4 mm flux gap modular machines has been conducted and the results are shown in Table 3. The data show that to maintain a similar winding temperature, the copper loss in the natural air cooled machine must be limited to 25 W. At this loss, the corresponding RMS current is 7.5 A, yielding an average torque of 1.6 Nm, which is approximately half of the forced-air-cooled counterpart. However, the natural air cooled machine has higher efficiency. This occurs because the average torque is proportional to the current, whereas the copper loss is proportional to the current squared. Therefore, when operating at a higher current to achieve more torque, the copper loss increases at a much faster rate. This disproportionate rise in loss relative to torque is what causes the efficiency of the forced air cooled machine to be lower, despite its superior power output.

3.2 | Influence of Flux Gap Width Under Constant Inlet Speeds

In the CFD simulations, the inlet boundary condition is set to a constant airflow speed of 10 m/s, corresponding to a mass flow rate of 1.12×10^{-5} kg/s, and a volumetric flow rate of 9.3×10^{-3} L/s per segment. The inlet air temperature is

TABLE 3 | Comparison between forced air cooled and natural air cooled modular FSPM machines (flux gap width = 4 mm).

	Forced air (10 m/s)	Natural air
Winding temperature	77.6°C	78.8°C
Copper loss	150.0 W	25.0 W
RMS current	18.4 A	7.5 A
Average torque	3.4 Nm	1.6 Nm
Power (@400 rpm)	141.9 W	65.9 W
Efficiency	48.6%	72.5%

maintained at 25°C, whereas the outlet boundary condition is set to a relative pressure of 0 Pa. The turbulence intensity chosen in CFX is 5% and a viscosity ratio is equal to 10. Additionally, the rotor speed in this section is fixed at 400 rpm, which is the machine's rated speed. It is important to note that varying the flux gap width comes at the expense of winding slot cross-sectional area, which also affects the end-winding surface. As the flux gap increases, the end-winding surface area decreases.

As an example, Figure 5 presents the temperature distribution of the modular FSPM at flux gap widths of 0 and 4 mm, and Figure 6 summarises the maximum winding and magnet temperatures at different flux gap widths. These two components are monitored as they are the most thermally vulnerable parts of a PM machine. The results indicate that the modular FSPM machine with a 1-mm flux gap achieves the lowest temperatures. A clear trend emerges where both winding and magnet temperatures increase with wider flux gaps. The nonmodular FSPM machine's temperature falls between that of the modular machines with 1 and 2 mm flux gaps. The PM temperature remains lower than the winding temperature since PM eddy current loss is not considered here. Instead, the magnets are primarily heated through thermal conduction from the windings. Despite this, the temperature difference between the winding and magnet remains relatively constant. Regarding the winding temperature, it is observed that the active winding reaches a higher maximum temperature compared to the front and rear end-windings. However, the front and rear end-winding temperatures are nearly identical.

In natural air-cooled machines, the active winding typically maintains lower temperatures because it efficiently dissipates

heat by thermal conduction via the stator iron core to the housing. In contrast, heat generated in the end-windings must first transfer to the active winding before being dissipated through the same conduction path. Although end-windings can also dissipate heat through air convection in the end space, the convection coefficient in natural cooling conditions is relatively low, making this cooling path inefficient. However, in forced air cooling, airflow enters the housing through the inlet and first blows over the front end-winding. After passing

through the active part of the machine, the air then flows over the rear end-winding, as the outlets are positioned to face the end-windings.

Figure 7 presents the average convection coefficients of the end-winding surfaces and flux gap surfaces at different flux gap widths. The convection coefficient is calculated using Equation (5), with a reference temperature set to 25°C, matching the inlet air temperature. According to Figure 7, when no flux gap is present, the convection coefficients of the front and rear end-windings are nearly identical.

However, the introduction of flux gaps significantly reduces the convection coefficient of the rear end-winding. This occurs because the flux gap alters the internal airflow pattern, diverting air through the flux gaps rather than forcing it to flow against the rear end-winding. Although the convection coefficients for both the front and rear end-windings decrease only slightly with a wider flux gap, the concurrent reduction in the end-winding area is likely the primary factor driving the overall temperature increase. Conversely, the convection coefficient within the flux gaps themselves is much higher than that of the end-windings. However, this coefficient decreases with a wider flux gap due to the reduced air velocity, as previously shown in Figure 8. For a narrow flux gap (e.g., 1 mm), the system achieves an optimal balance. Although airflow velocity is unavoidably reduced, the positive influence of the new, high-convection heat dissipation area provided by the flux gap outweighs the negative impact of the slower flow. This explains the minimum
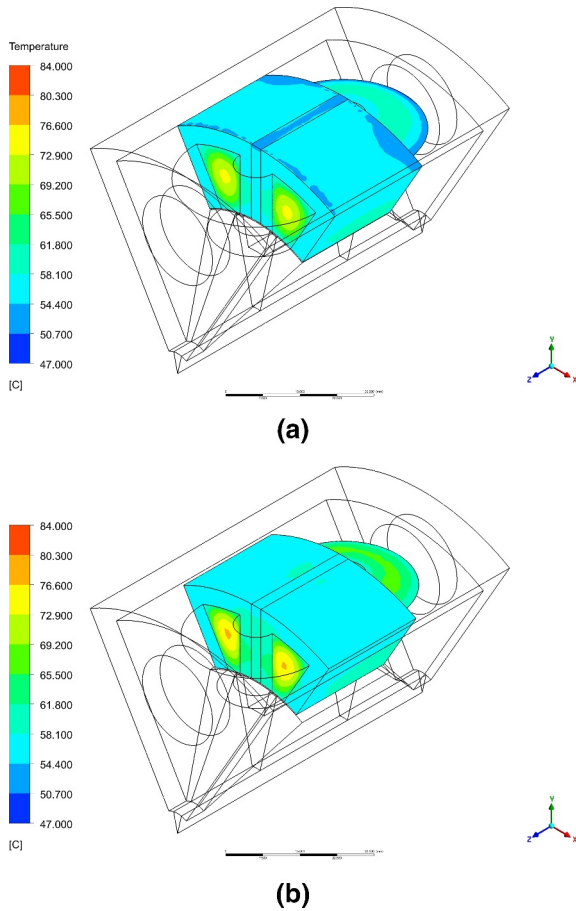

FIGURE 5 | Temperature distribution of the modular FSPM machine with a flux gap width at (a) 0 mm and (b) 4 mm when the inlet speed is 10 m/s.
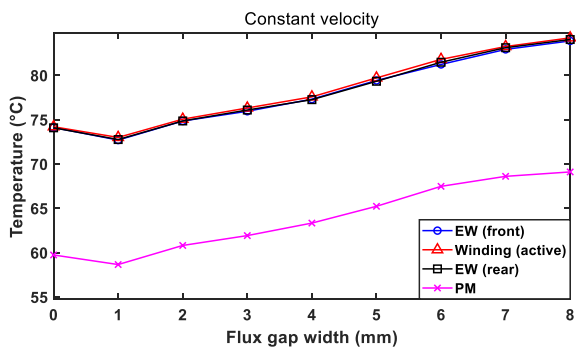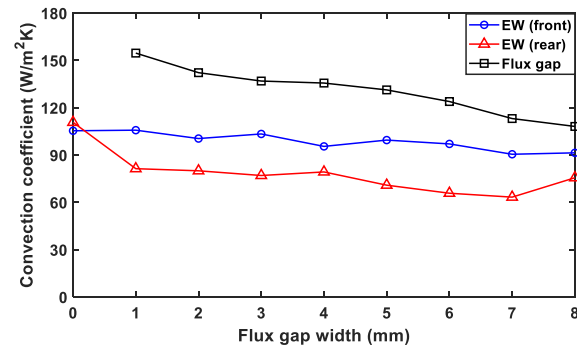

FIGURE 7 | Convection coefficient of end-winding and flux gap surfaces versus flux gap widths when the inlet speed is 10 m/s.
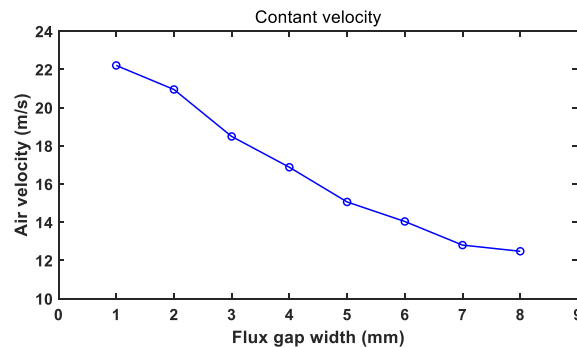

FIGURE 6 | Maximum temperatures versus flux gap width when the inlet speed is 10 m/s.

FIGURE 8 | Average air velocity of flux gaps versus flux gap when the inlet speed is 10 m/s.

temperature at the 1-mm width. As the gap widens further, the combined effect of a continuously shrinking end-winding area and a declining flux gap convection coefficient leads to the observed rise in machine temperature.

Although the presence of flux gaps negatively impacts the thermal performance of the modular FSPM machine under the same inlet speed, it significantly reduces system pressure loss as the flux gap width increases, as shown in Figure 9. According to Equation (8) [27], when the inlet speed and cross-sectional area of the inlet remain constant, the volumetric flow rate (Q) does not change. Consequently, the machine's flow resistance is directly proportional to the system pressure loss. A reduction in pressure loss indicates a corresponding decrease in flow resistance. This helps reduce the power consumed by the air pump. In addition, the required system power of the whole machine can be calculated using (Equation (9)) and is also illustrated in Figure 9.

$$\Delta p = R_f Q^2 \tag{8}$$

$$P_{\text{fluid}} = \Delta p \cdot Q \tag{9}$$

where R_f represents the system flow resistance and Q means the volumetric flow rate. The fluid power (P_{fluid}) is a function of both the volumetric flow rate (Q) and the system pressure loss (Δp). It can be seen that the pumping power reduces significantly from 17.6 to 3.8 W as the flux gap width increases.

The fluid behaviour shown in Figure 10 in the modular FSPM machine follows a series of distinct stages: (1) When air enters the front-end space of the machine from a narrow inlet, it undergoes a sudden expansion, leading to a separation loss. (2) The air then contracts as it flows into the air gap and flux gap, with a separation loss. (3) As the air moves through the air gap and flux gap, rotor rotation introduces additional frictional and shock losses. (4) Finally, the air exits the machine, experiencing expansion into the end space followed by contraction at the outlet, mirroring the inlet flow process. According to Equation (9) [27], the fluid power P_{fluid} required to drive the fluid is related to the volumetric flow rate Q and system pressure loss Δp. Since the volumetric flow rate remains constant, a decrease in pressure loss translates to reduced fluid power requirements. Therefore, as the flux gap width increases, the required fluid power decreases accordingly.
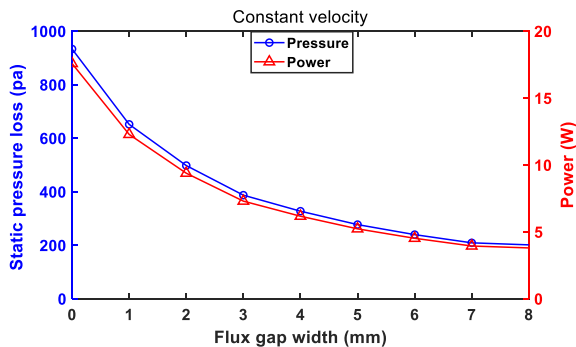
3.3 | Influence of Flux Gap Width Under Constant Pressure Loss

In Section 3, it was observed that under a constant inlet flow rate, flux gaps negatively impact the thermal performance of the modular FSPM machine, despite significant variations in pressure loss at different flux gap widths. However, the effect of flux gap width under a fixed pressure loss has not yet been considered. To address this, another series of CFD simulations is conducted, where a constant 500 Pa pressure drop is imposed between the inlets and outlets.

Figures 11 and 12 present the maximum winding and magnet temperatures under a constant pressure loss. The results indicate that the introduction of flux gaps significantly reduces machine temperature, reaching its minimum at a flux gap width of 4 mm. However, as the flux gap width increases from 5 to 8 mm, the machine temperature rises slightly. Consistent with the findings from the previous sections, the temperature difference between the winding and magnet remains relatively constant. Focusing on the winding temperature, the active winding region exhibits slightly higher temperatures than the front and rear end-windings. Although the front and rear end-winding temperatures are nearly identical.

To better understand the factors influencing the thermal performance, it is necessary to analyse the convection coefficients of the machine components. Figure 13 presents the average convection coefficients of the end-winding surfaces and flux gap surfaces at different flux gap widths. The results show that the convection coefficients of the front end-winding surfaces are consistently higher than those of the rear end-winding surfaces, and their values remain relatively stable as the flux gap width changes. Some fluctuations are observed, which may be attributed to variations in mesh quality, as each flux gap width corresponds to a different CFD model. For the flux gap surfaces, the convection coefficient increases rapidly when the flux gap width expands from 1 to 4 mm, followed by a slight increase from 4 to 8 mm. As seen in Figure 13, incorporating flux gaps is an effective cooling method, explaining the sharp temperature reduction observed in Figure 12 when the flux gap is introduced. Additionally, the rapid increase in the convection coefficient between 1 and 4 mm corresponds to the minimum machine temperature at 4 mm. However, the observed temperature rise from 4 to 8 mm
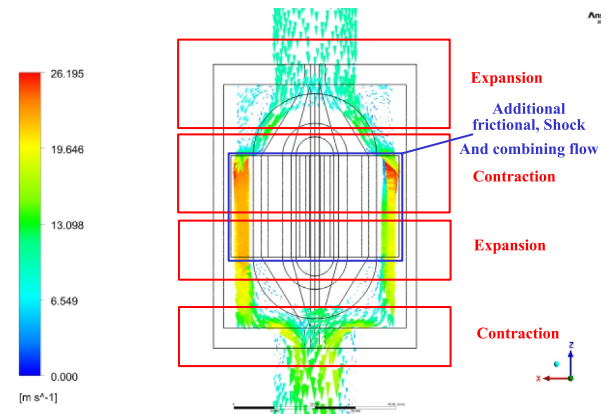
FIGURE 9 | Pressure losses and air power versus flux gap widths when the inlet speed is 10 m/s.

FIGURE 10 | Fluid behaviour in the modular FSPM machine.

cannot be explained solely by changes in the convection coefficient. In this case, modifications to the machine model must be considered. As mentioned in Section 3.2, increasing the flux gap width reduces the winding slot cross-sectional area, leading to a decrease in the end-winding outer surface area. With a smaller outer surface area and an unchanged convection coefficient, the machine's ability to dissipate heat diminishes, explaining the temperature rise from 4 to 8 mm.
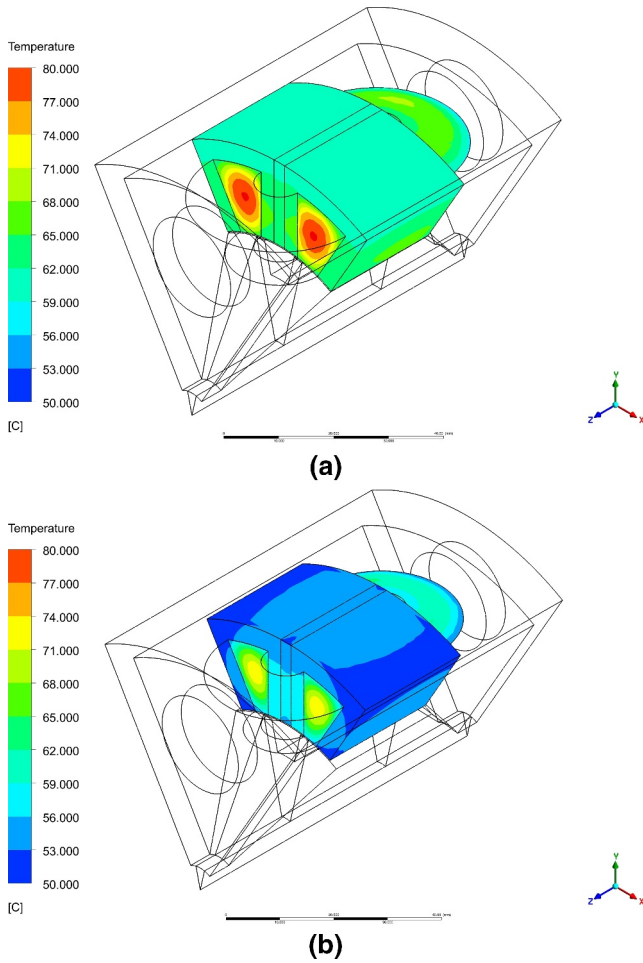

(a)

(b)

FIGURE 11 | Temperature distribution of the modular FSPM machine with a flux gap width at (a) 0 mm and (b) 4 mm when the inlet pressure is 500 pa.
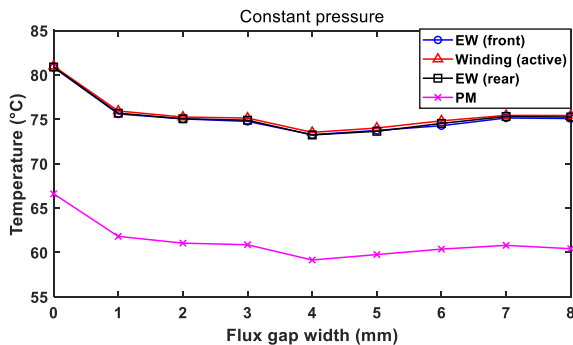

FIGURE 12 | Maximum temperatures versus flux gap width when the inlet pressure is 500 pa.

Figure 14 illustrates the inlet air velocity and required system power of the whole machine. As discussed in Section 3.2, increasing the flux gap width reduces system flow resistance. According to Equation (8), when the total pressure loss remains constant, a reduction in flow resistance leads to a higher volumetric flow rate. In this case, the increased volumetric flow rate results in a higher inlet air velocity. Meanwhile, the required power increases from 6.6 to 14.8 W as the flux gap gets wider.

3.4 | Influence of Flux Gap Width Under Constant Torque and Fan Power

Previous simulations assumed a fixed copper loss, resulting in variable resistance, current and, consequently, variable average torque across different flux gap widths. Furthermore, because airflow (Q) and pressure loss (Δp) are strongly coupled, with fan power (P) being the result of their interaction, the required external fan power also varies with the flux gap, as shown in Figures 9 and 14. To enable a fair comparison of thermal performance, this section will analyse the models under conditions of fixed average output torque and fixed external fan power.

For the analysis in this section, the modular FSPM machine's average output torque is held constant at 2.75 Nm. This is achieved by calibrating the injected current according to the flux gap width, with the specific values listed in Table 4. With the
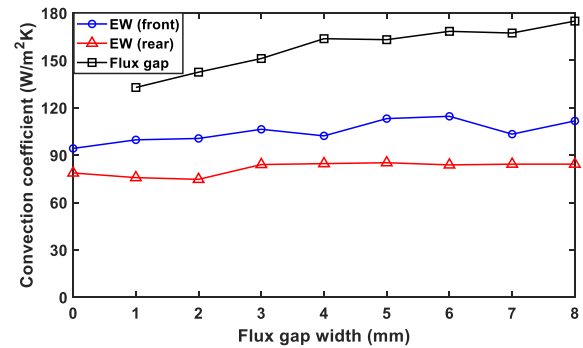

FIGURE 13 | Convection coefficient of end-winding (EW) and flux gap surfaces versus flux gap widths when the inlet pressure is 500 pa.
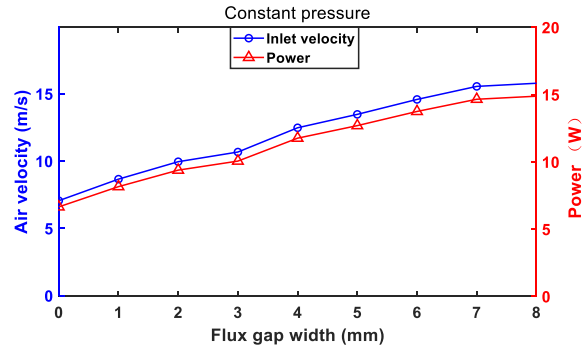

FIGURE 14 | Inlet velocity and air power versus flux gap widths when the inlet pressure is 500 pa.

TABLE 4 | Copper loss and efficiency of modular FSPM at the same output torque at 400 rpm.

| Flux gap (mm)	RMS current (A)	Copper loss (W)	Efficiency (%)
0	28.3	294.8	28.1
1	21.2	172.9	39.9
2	17.7	125.4	47.9
3	15.6	102.2	53.0
4	14.1	89.1	56.4
5	13.1	80.7	58.8
6	12.7	81.5	58.6
7	12.7	87.5	56.8
8	13.4	105.5	52.2

machine operating at 400 rpm, the corresponding output power is given by

$$P_{out} = T_{ave} \cdot \omega \tag{10}$$

where P_{out} is output power, T_{ave} is the average torque and ω is the angular speed, yielding a value of 115.2 W. At this low operational speed, PM eddy current and iron losses are negligible; thus, the efficiency for each configuration is listed in Table 4. The results show that although the nonmodular FSPM machine has the largest slot area, it requires a significantly higher current to achieve the same output torque. This leads to substantially higher copper loss and, consequently, lower efficiency compared to the modular machines. Among the modular designs, the 5-mm flux gap topology achieves the highest efficiency, as it requires the lowest current and thus the lowest copper loss to produce the target torque. It is worth noting that the efficiencies of these machines are relatively low due to the small fill factor, as observed in some existing laboratory prototypes where smaller copper wires were deliberately used to simplify the winding process.

For the CFD modelling, the external fan power was set to 10 W, with the corresponding inlet condition calculated using Equations (8) and (9). Figure 15 presents the maximum winding and magnet temperatures under constant output torque and fan power. The results show that the nonmodular FSPM machine operates at a significantly higher temperature than the modular machines with flux gaps. This superior thermal performance is due to two key factors: firstly, the flux gap provides an additional surface area for heat dissipation, and secondly, by improving the winding factor, the flux gap reduces the required current and consequently the copper loss.

Consistent with previous findings, an optimal flux gap width of 5 mm minimises the machine temperature. This optimum represents a trade-off between electromagnetic and thermal performance. As Figure 4 and Table 4 indicate, the 5-mm gap is optimal for electromagnetic performance (e.g., torque). Although a 4-mm gap is thermally optimal (Figure 12), the machine with a 5-mm gap exhibits only a marginally higher temperature. Therefore, considering the combined electromagnetic and thermal performance, the 5-mm flux gap is identified as the overall optimal design for this modular FSPM machine.
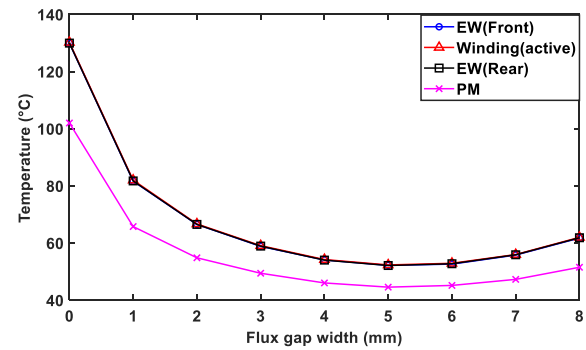
FIGURE 15 | Maximum temperatures versus flux gap width at the same output torque and fan power.

3.5 | Influence of Rotor Speed Under the Same Inlet Air Speed

As stated in ref. [32], rotor rotation introduces additional pressure loss in electrical machines. In the case of the modular FSPM machine, there are two key differences compared to traditional PM machines: (1) In conventional PM machines, whether SPM or IPM, the rotor is typically nonsalient. In contrast, the FSPM machine features a salient rotor structure, which adds complexity to the airflow within the air gap. (2) The modular FSPM machine includes flux gaps, where airflow behaviour can be significantly influenced by rotor speed. To investigate these effects, several CFD simulations are conducted at different rotor speeds, ranging from 400 to 3600 rpm. The modular FSPM machine with a 4-mm flux gap width, as detailed in Section 2.1, is used for these simulations. The inlet and outlet boundary conditions remain unchanged from Section 3.4, ensuring that variations in system pressure loss directly reflect changes in flow resistance. The relationship between pressure loss and rotor speed is shown in Figure 16. The results indicate that as rotor speed increases, the system's total pressure loss also rises, leading to an increase in flow resistance. However, compared to the effect of changes in the flux gap width, rotor speed has a relatively smaller impact on system pressure loss.

The rotor's rotation affects not only the system pressure loss but also the temperature of machine components. Figures 17 and 18 show the maximum winding and magnet temperatures at different rotor speeds. The results show that machine
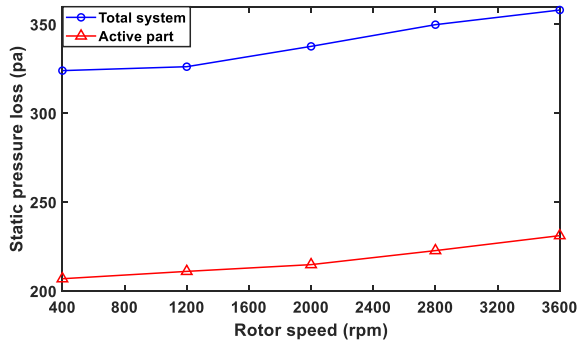
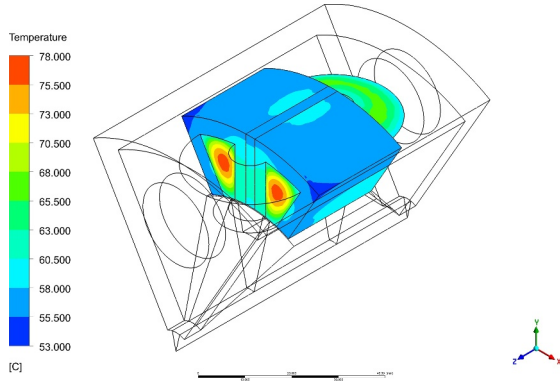**FIGURE 16** | Pressure losses versus rotor speed when the inlet speed is 10 m/s.

FIGURE 17 | Temperature distribution of the modular FSPM machine with rotor speed at 400 rpm when the inlet speed is 10 m/s.
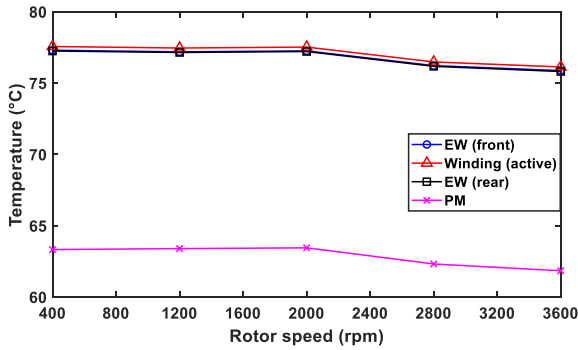

FIGURE 18 | Maximum temperatures of the machine versus rotor speed when the inlet speed is 10 m/s.

temperatures remain steady at relatively low speeds, from 400 to 2000 rpm. However, when the rotor speed exceeds 2800 rpm, a noticeable temperature reduction occurs, and temperatures continue to decrease as the speed increases to 3600 rpm. Regarding the PM temperature, it remains lower than the winding temperature, with the temperature difference between the two components staying relatively constant.

The variation in machine temperature can be explained by the convection coefficients of the end-winding and flux gap regions, as shown in Figure 19. The temperature reduction is not influenced by the convection of the front end-winding, as its convection coefficient remains nearly unchanged with increasing
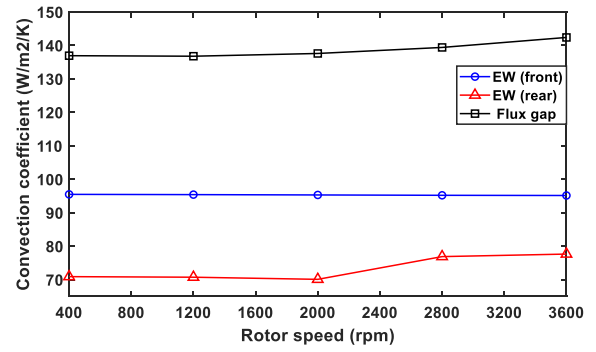

FIGURE 19 | Convection coefficient of end-winding and flux gap surfaces versus rotor speed when the inlet speed is 10 m/s.

rotor speed. However, in the flux gap region, the convection coefficient continuously increases as rotor speed rises from 400 to 3600 rpm. The primary cause of the temperature drop at 2800 rpm is the sudden increase in the convection coefficient of the rear end-winding. From 400 to 2000 rpm, this coefficient remains nearly constant, but at 2800 rpm, it experiences a sharp increase. Figure 20 illustrates that as rotor speed increases, the air exiting the air gap tends to flow through the rear end-winding. This is known as the combining flow phenomenon as described in ref. [28]. Beyond this point, as the rotor speed continues to rise to 3600 rpm, the convection coefficient of the rear end-winding increases only slightly. The continued temperature reduction from 2800 to 3600 rpm is primarily attributed to the increasing convection coefficient in the flux gap region.

3.6 | Influence of Rotor Speed With Iron and PM Losses

As aforementioned, in Section 3.5, the winding and PM temperatures were obtained without considering the stator iron loss, rotor iron loss or PM eddy current loss to allow the cooling effectiveness to be more clearly observed through winding temperature variations. However, these losses are crucial for accurately predicting the actual temperature distribution within the investigated machine. Therefore, they have been calculated using 2D FEA simulations (JMAG software package), as shown in Figure 21. The results show that these losses increase noticeably with rotor speed. Among them, stator iron loss is the most significant one, whereas rotor iron loss and PM eddy current loss are comparatively smaller. Both stator and rotor iron losses tend to rise gradually as the flux gap width increases. In contrast, PM eddy current loss is the highest when the flux gap width is 0 mm, decreases steadily to its lowest value at 6 mm and then increases again as the flux gap width expands to 8 mm.

As an example, the losses at a flux gap width of 4 mm have been incorporated into the CFD models, and the resulting maximum winding and PM temperatures with iron and PM eddy current loss are presented in Figure 22. Different from the results shown in Figure 18 without considering iron and PM eddy current losses, the results here show that both winding and magnet temperatures exhibit a slight upward trend with speed, primarily driven by increasing iron and PM eddy current losses due to increase in rotor speed. However, the relationship is nonlinear,
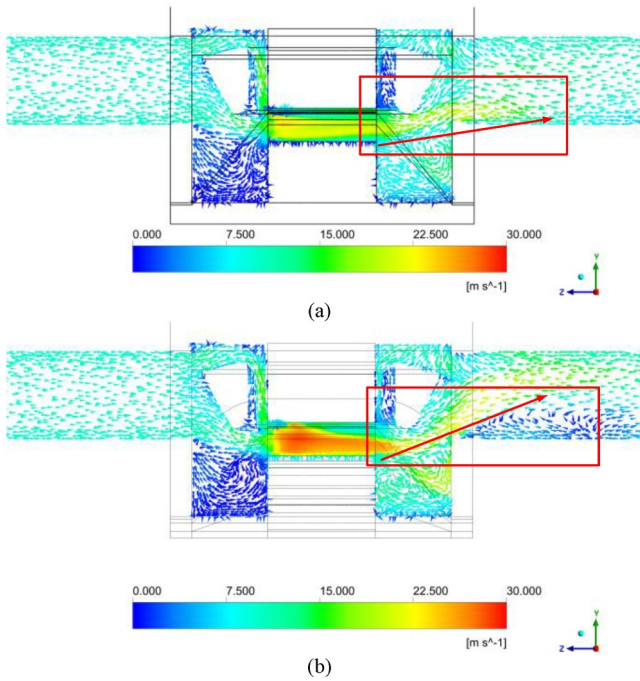
FIGURE 20 | Air velocity vector distributions in the axial direction of the modular FSPM at (a) 400 rpm and (b) 3600 rpm.

as higher rotor speeds also alter the internal airflow and enhance convective heat transfer. As explained in Section 3.5, the 'combining flow' at high speeds is directed through the rear end-winding, significantly improving heat dissipation. This effect leads to a noticeable, nonlinear temperature drop (see Figure 18) at specific speeds, such as 2800 rpm, which is difficult to capture with simple analytical equations.

In summary, the thermal performance of the modular FSPM at high speed is a balance of competing effects. The dominant heating factors are the iron and PM eddy current losses, which scale with speed or its square. Conversely, the enhanced cooling from the high-speed combining flow counteracts this, mitigating the temperature rise, particularly in the windings.

4 | Experimental Validation

In order to verify the accuracy of the CFD thermal models, relevant thermal experiments have also been carried out in this paper. The thermal experiments can be divided into two parts: natural air cooling and forced air cooling and will be discussed in the following sections.

4.1 | Natural Air-Cooling Experiments

The natural cooling experiments aim at identifying key thermal parameters needed for the forced air-cooling experiments in Section 4.2. There are several important conditions that need to be explained in the experiments. Firstly, only DC copper loss is introduced, though losses in electrical machines include copper loss, iron loss and PM eddy current loss. It is because that the DC copper loss is the most controllable loss, whereas the
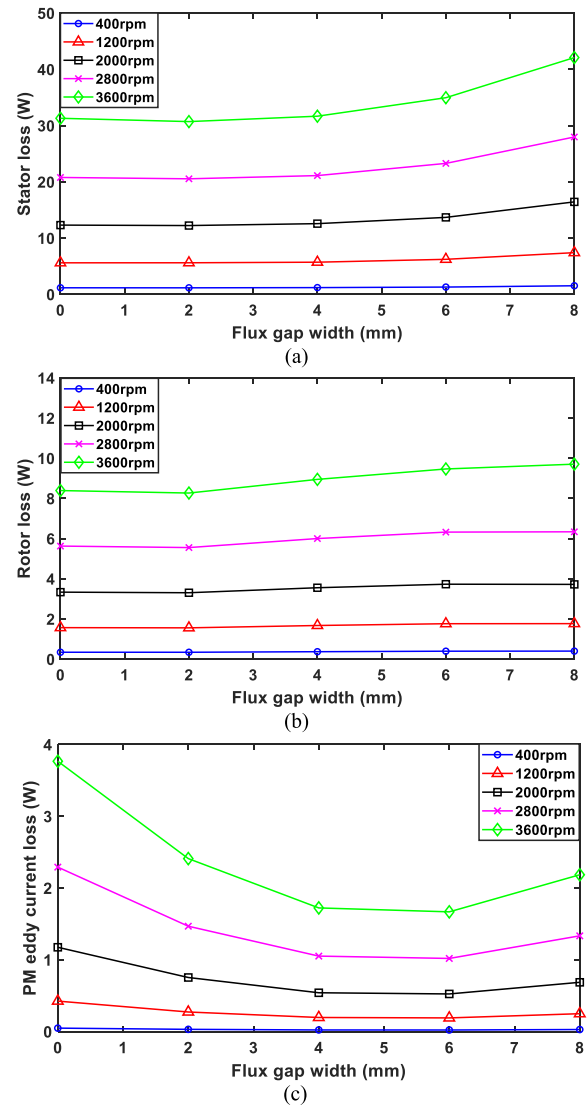

FIGURE 21 | Losses at different rotor speeds and different flux gap widths. (a) Stator iron loss, (b) rotor iron loss and (c) PM eddy current loss.
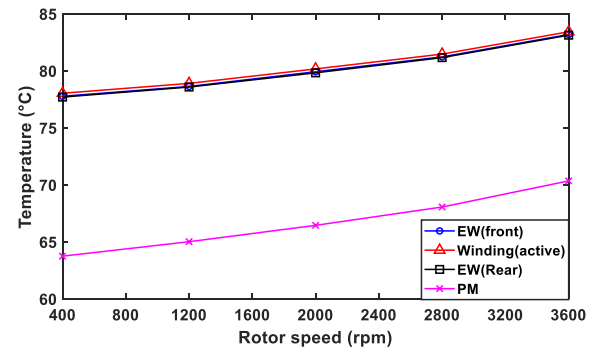

FIGURE 22 | Maximum temperatures of the machine versus rotor speed when iron loss and PM eddy current loss are considered.

accuracy of other losses from measurements remains uncertain. This experiment is mainly intended to validate the correctness of the thermal model, so introducing other losses only brings more uncertainties to the experiment. Secondly, the metal rotors

are replaced by a 3D-printed polylactic acid (PLA) rotor, as shown in Figure 23. The reason for using a nonmagnetic 3D-printed PLA rotor is because the existing drive motor in the test rig is not powerful enough to drive the prototype to a rather high rotation speed. With the laminated rotor, the prototype can only be operated at around 100 rpm, which makes it difficult to observe any meaningful temperature changes at different rotor speeds. Since the rotor's sole function is to generate air turbulence within the enclosed housing, its material has little influence on the thermal performance. As a result, using a 3D-printed PLA rotor does not compromise the accuracy of the experiment. This setup enables the rotor speed to reach approximately 1000 rpm. Accordingly, in this experiment, the temperatures of the machine components are recorded at 0, 400 and 800 rpm.

Figure 24 shows the test rig for testing natural cooling performance. The inverter used in the test rig is *Texas Instruments* 'DRV8301-69M-KIT', which is used to drive the brushless AC motor. The power supply shown here is to inject DC current. The DC loss of the system is set to be 44 W, which is realised by the power limit function of the power supply. The temperatures of each machine component are monitored by thermal couples (T-type and K-type) placed in the prototype machine. There are three thermal couples buried in the three coils of different phases during the winding process. The other thermal couples are attached to the stator, magnet, housing, endcap and the last one is exposed to the ambient to monitor the temperature of the laboratory.
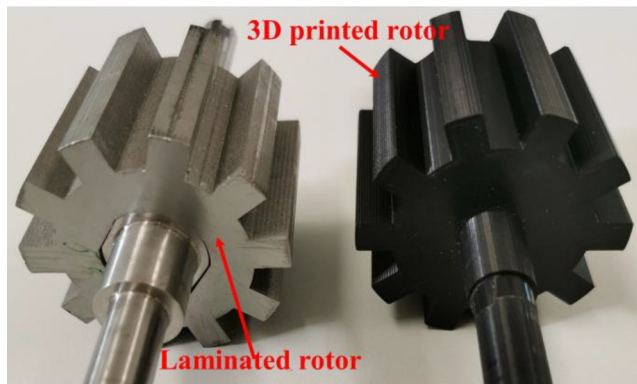
For the natural cooling experiment, it is essential to define a combined coefficient on the machine outer surface, which includes thermal convection coefficient and thermal radiation coefficient. In general, for the natural cooling, the convection coefficient should be between 5 W/m²·K and 15 W/m²·K. However, there is an air conditioner in the laboratory, where the experiments are conducted; hence, the actual convection coefficient is supposed to be much higher. Therefore, an additional experiment is conducted to determine the convection coefficient. It was observed that the frame to which the prototype is mounted also contributes to heat dissipation, leading to significantly lower temperatures at the end caps in contact with the frame compared with the housing. To simulate an adiabatic boundary condition, both end caps were replaced with wooden boards (see Figure 25), effectively minimising heat transfer through these surfaces. At the same time, the rotor is also removed, leaving only stator iron core and coils in the housing. The corresponding CFD model has been built, and the convection coefficient of the housing surface is retuned to match the measured results. The essential thermal conductivities in W/m·K of the solid components used in CFD simulations are 168 for the housing, 30 for the stator iron core, 95.26 (axial) and 0.39 (radial) for the winding, 7.6 for the magnet and 0.18 for the 3D printed PLA rotor. It is worth noting that in the experimental section, the thermal conductivity of the winding is lower than that used in the simulation sections. This is mainly because the laboratory prototype was not vacuum-impregnated, which resulted in a reduced effective thermal conductivity. The final
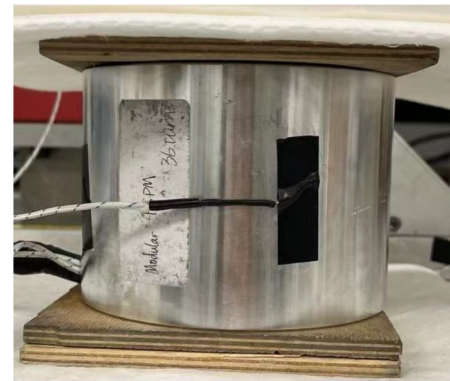

FIGURE 23 | Laminated iron core rotor and 3D-printed PLA rotor.

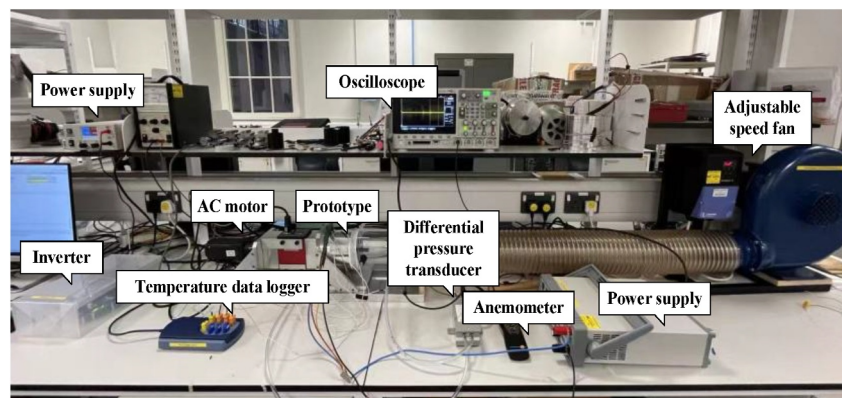**FIGURE 25** | Measuring convection coefficient on housing surface.

FIGURE 24 | Test rig for natural and forced air-cooling experiments.

obtained combined coefficient on the housing surface under the laboratory condition is 22 W/m^2·K.

After introducing the essential parameters of the experiment, Figure 26 shows the measured temperatures at different rotor speeds. The coil temperatures decrease slightly as the rotor speed increases, whereas the temperatures of the stator or housing remain stable. It should be noted that the temperatures obtained from the simulations are average temperatures of these components. The difference between the simulations and experiments is partly due to the location of the thermal couples. The surface temperatures of the stator and housing are slightly lower than those at the centre. As for the coils, the centre temperature could be much higher than its surface temperature. Therefore, considering the uncertain positions where the thermal couples are buried in the slot, the difference between measurement and simulation is unavoidable. More importantly, the predicted and measured temperatures exhibit the same trend as the rotor speed increases. For the other components, the discrepancies may be attributed to poor contact between the thermocouples and the measurement points.

4.2 | Forced Air-Cooling Experiments

A series of forced air-cooling experiments have also been carried out to validate the prediction concerning the relationship between machine temperature and air flow velocity. In this section, the modular FSPM machine is used and there are six opening holes on each end cap as inlets and outlets. The basic experimental conditions are the same as the previous natural air-cooling experiments, but several extra equipment has been used as shown in Figure 24. Firstly, a centrifugal fan (*L-28-E*), manufactured by *B.O.B Stevenson Ltd,* is connected to the prototype with a long tube to provide a relatively stable air flow to cool the machines. The fan is controlled by an *OPTI-DRIVE E3* inverter which allows the fan to rotate from 0 to 2500 rpm. In addition, a differential pressure transducer, *PX277-005D5V,* made by *OMEGA,* is used to measure the pressure difference between the upstream and downstream of the prototypes. One end of the pressure sensor is connected to the tube between the prototype and the fan, whereas the other end is exposed to the ambient representing the standard atmospheric pressure. The air flow velocity between the fan and

the machine is important to validate the simulation and experiment. To measure this, an anemometer (*testo 425*) is employed in the test rig. The probe of the anemometer is inserted into the tube to measure the air velocity.

Although the fan speed is known and adjustable, the airflow velocity within the tube must be measured using an anemometer. Figure 27 illustrates the relationship between fan speed and measured airflow velocity, as well as the simulated and measured pressure losses for the modular FSPM machine. The results show that the air flow velocity in both machines is nearly proportional to the fan speed. Regarding the pressure losses, discrepancies between simulation and measurement are likely attributable to the accuracy limitations of the anemometer and the differential pressure transducer.

The following experiments measure the temperatures of the modular FSPM machines at different air velocities, with the total system loss (copper loss) maintained at 44 W. The results, shown in Figure 28, indicate that the forced air cooling rapidly reduces machine temperatures to around 30°C. The measured stator and housing temperatures align closely with the simulation results. However, the measured coil temperature is lower than the simulated value at relatively high air velocities. This discrepancy is likely due to the prototype winding not being impregnated and having a low slot fill factor of approximately 0.2. As a result, numerous gaps exist inside the slots and between copper wires, creating additional cooling channels not
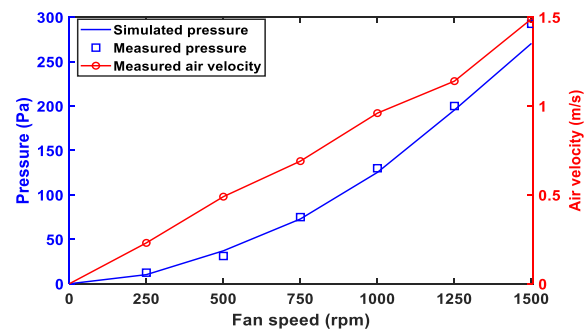
FIGURE 27 | Measured air velocity, measured and simulated pressures at different fan speeds for the modular FSPM machines @ rotor speed of 400 rpm.

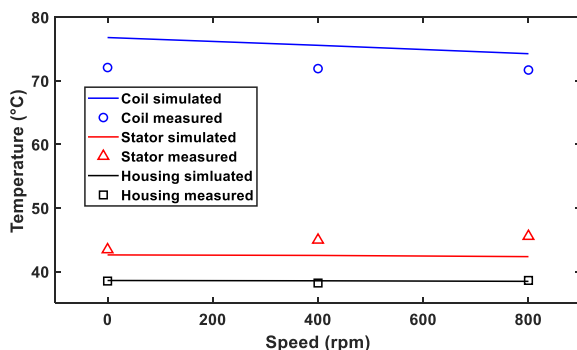**FIGURE 26** | Simulated and measured temperatures of the modular FSPM machine at different rotor speeds.
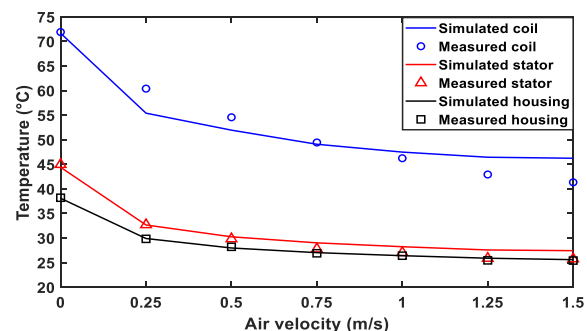
FIGURE 28 | Simulated and measured temperatures at different air velocities of the modular FSPM machine @ rotor speed of 400 rpm.

accounted for in the CFD model. Consequently, the coils can dissipate more heat than predicted.

5 | Conclusion

In this paper, a forced air-cooling system has been implemented for the modular FSPM machine. This machine benefits from the extra cooling channels provided by the flux gaps between stator segments. To examine the key parameters influencing the cooling efficiency, a series of CFD simulations have been conducted. Given the significant impact of the flux gap width on the thermal performance of the modular FSPM machine, multiple nonmodular and modular FSPM machine models with varying flux gap widths have been developed and analysed. The study also explores the effect of the flux gap width on the thermal performance of forced air-cooled modular FSPM machines under different inlet conditions. Additionally, since rotor speed also affects thermal performance, the impact of rotor speed on the forced air-cooling efficiency has been investigated as well. The study reveals that at a constant inlet air speed, the modular structure lowers the machine temperature only at a small flux gap (e.g., 1 mm). Beyond this point, the temperature increases with wider flux gaps, eventually exceeding that of the nonmodular FSPM machine. This temperature increase is primarily attributed to a significant reduction in the rear end-winding convection coefficient. Additionally, the convection coefficients of both the front end-winding and the flux gap decrease as the flux gap widens. This phenomenon occurs because the system flow resistance decreases with increasing flux gap width, leading to a reduction in air velocity since the volumetric flow rate remains constant. The lower air velocity limits the cooling effectiveness of the forced air-cooling system.

However, when the total system pressure loss is held constant, the cooling system is found to be most effective at a flux gap width of 4 mm. Although both excessively narrow and excessively wide flux gaps negatively impact the cooling performance, the modular FSPM machines still exhibit significantly lower temperatures than the nonmodular FSPM machines. The temperature increase at wider flux gaps is primarily due to the reduction in the end-winding surface area. Lastly, the study shows that at low rotor speeds, machine temperatures remain nearly constant. However, once the rotor speed reaches 2800 rpm, a noticeable temperature reduction occurs. Additionally, as rotor speed increases, the system pressure loss also rises.

Conflicts of Interest

The authors declare no conflicts of interest.

Data Availability Statement

Data available on request due to privacy/ethical restrictions.

References

1. D. G. Dorrell, M.-F. Hsieh, M. Popescu, L. Evans, D. A. Staton, and V. Grout, "A Review of the Design Issues and Techniques for Radial-Flux Brushless Surface and Internal Rare-Earth Permanent-Magnet Motors," *IEEE Transactions on Industrial Electronics* 58, no. 9 (2010): 3741–3757, https://doi.org/10.1109/tie.2010.2089940.

2. Y. Yang, B. Bilgin, M. Kasprzak, et al., "Thermal Management of Electric Machines," *IET Electrical Systems in Transportation* 7, no. 2 (2017): 104–116, https://doi.org/10.1049/iet-est.2015.0050.

3. D. Staton, E. Chong, S. Pickering, and A. Boglietti, *Cooling of Rotating Electrical Machines, Fundamentals, Modelling, Testing and Design* (IET, 2022).

4. C. Kral, A. Haumer, M. Haigis, H. Lang, and H. Kapeller, "Comparison of a CFD Analysis and a Thermal Equivalent Circuit Model of a TEFC Induction Machine With Measurements," *IEEE Transactions on Energy Conversion* 24, no. 4 (2009): 809–818, https://doi.org/10.1109/tec.2009.2025428.

5. M. Roffi, F. J. Ferreira, and A. T. De Almeida, "Comparison of Different Cooling Fan Designs for Electric Motors," in *2017 IEEE International Electric Machines and Drives Conference (IEMDC)* (IEEE, 2017), 1–7.

6. T. Jercic, D. Zarko, M. Martinovic, et al., "Centrifugal Fan Design for Permanent Magnet Synchronous Motor in a Traction Application," in *2017 IEEE International Electric Machines and Drives Conference (IEMDC)* (IEEE, 2017), 1–7.

7. C. Jang, J. Lee, M. Sung, and J. Lee, "Optimal Design of Cooling Fan for 200 kW Class Low Voltage Motor by Numerical Analysis," in *2019 IEEE International Electric Machines & Drives Conference (IEMDC)* (IEEE, 2019), 1163–1168.

8. S. Goh, A. S. Fawzal, K. N. Gyftakis, and A. J. Cardoso, "Impact of the Fan Design and Rotational Direction on the Thermal Characteristics of Induction Motors," in *2018 13th International Conference on Electrical Machines (ICEM)* (IEEE, 2018), 1227–1233.

9. M. Satrústegui, G. Artetxe, I. Elosegui, M. Martinez-Iturralde, and J. C. Ramos, "Wafter Design for Totally Enclosed Electric Machines," *Applied Thermal Engineering* 129 (2018): 93–105, https://doi.org/10.1016/j.applthermaleng.2017.10.011.

10. A. Boglietti and A. Cavagnino, "Analysis of the Endwinding Cooling Effects in TEFC Induction Motors," in *Conference Record of the 2006 IEEE Industry Applications Conference 41st IAS Annual Meeting*, Vol. 2 (IEEE, 2006), 797–804, https://doi.org/10.1109/ias.2006.256617.

11. M. Hettegger, B. Streibl, O. Biro, and H. Neudorfer, "Measurements and Simulations of the Convective Heat Transfer Coefficients on the End Windings of an Electrical Machine," *IEEE Transactions on Industrial Electronics* 59, no. 5 (2011): 2299–2308, https://doi.org/10.1109/tie.2011.2161656.

12. S. Ding, J. Liu, and L. Zhang, "Fan Characteristics of the Self-Support Components of Rotor Ends and Its Performance Matching," *International Journal of Heat and Mass Transfer* 108 (2017): 1917–1923, https://doi.org/10.1016/j.ijheatmasstransfer.2016.12.005.

13. Y. Gai, M. Kimiabeigi, Y. C. Chong, et al., "Cooling of Automotive Traction Motors: Schemes, Examples, and Computation Methods," *IEEE Transactions on Industrial Electronics* 66, no. 3 (2018): 1681–1692, https://ieeexplore.ieee.org/document/8369353.

14. J. Wen and J. Zheng, "Numerical Analysis of the External Wind Path for Medium-Size High-Voltage Asynchronous Motors," *Applied Thermal*

Engineering 90 (2015): 869–878, https://doi.org/10.1016/j.applthermaleng.2015.07.065.

15. C. Juncil, W. Zhigang, L. Weili, et al., "Influence of Axial Ventilation Structures on Electromagnetic Field and Heat Transfer of Traction Motor Used for High—Speed EMU," in *2017 20th International Conference on Electrical Machines and Systems (ICEMS)* (IEEE, 2017), 1–6.

16. K. Bersch, S. Nuzzo, P. Connor, et al., "Combined Thermofluid and Electromagnetic Optimisation of Stator Vent Cooling," in *2018 13th International Conference on Electrical Machines (ICEM)* (IEEE, 2018), 1116–1122.

17. X. Fan, R. Qu, J. Li, D. Li, B. Zhang, and C. Wang, "Ventilation and Thermal Improvement of Radial Forced Air-Cooled FSCW Permanent Magnet Synchronous Wind Generators," *IEEE Transactions on Industry Applications* 53, no. 4 (2017): 3447–3456, https://doi.org/10.1109/tia.2017.2686350.

18. H. Ding, W. Sixel, C. Temme, and B. Sarlioglu, "Design of a Flux-Switching PM Machine With Axial Fan Capability," in *2018 IEEE International Conference on Electrical Systems for Aircraft, Railway, Ship Propulsion and Road Vehicles & International Transportation Electrification Conference (ESARS-ITEC)* (IEEE, 2018), 1–6.

19. R. L. Owen, Z. Zhu, A. S. Thomas, G. W. Jewell, and D. Howe, "Alternate Poles Wound Flux-Switching Permanent-Magnet Brushless AC Machines," *IEEE Transactions on Industry Applications* 46, no. 2 (2010): 790–797, https://doi.org/10.1109/tia.2009.2039913.

20. M. Cheng, W. Hua, J. Zhang, and W. Zhao, "Overview of Stator-Permanent Magnet Brushless Machines," *IEEE Transactions on Industrial Electronics* 58, no. 11 (2011): 5087–5101, https://doi.org/10.1109/tie.2011.2123853.

21. G. Zhang and G. Li, "Comparative Study of Stator-Mounted PM Machines Focusing on Thermal Performance," in *2023 IEEE International Electric Machines & Drives Conference (IEMDC)* (IEEE, 2023), 1–7.

22. R. Zhou, G. Li, Z. Zhu, M. Foster, and D. Stone, "Improved Cooling in Modular Consequent Pole PM Machine Utilizing Flux Gaps," in *2020 IEEE Energy Conversion Congress and Exposition (ECCE)* (IEEE, 2020), 4253–4260.

23. R. Zhou, G. Li, Z. Zhu, et al., "Novel Liquid Cooling Technology for Modular Consequent-Pole PM Machines," in *2021 IEEE International Electric Machines & Drives Conference (IEMDC)* (IEEE, 2021), 1–7.

24. W. Zhang, G. Li, Z. Zhu, B. Ren, and Y. Chong, "New Ventilation Cooling for Modular PM Machines Utilizing Flux Gaps and Rotor Ducts," *IEEE Transactions on Energy Conversion* 39, no. 4 (2024): 2718–2727, https://doi.org/10.1109/tec.2024.3382491.

25. W. Zhang, G. Li, Z. Zhu, B. Ren, and Y. Chong, "Semi-Flooded Cooling for High Torque Density Modular Permanent Magnet Machines," *IET Electric Power Applications* 18, no. 7 (2024): 756–765, https://doi.org/10.1049/elp2.12432.

26. G. Zhang and G. Li, "Performance Comparison of Optimized Stator-Mounted Permanent Magnet Machines Focusing on PM Usage," in *2022 IEEE Energy Conversion Congress and Exposition (ECCE)* (IEEE, 2022), 1–7.

27. D. Staton, E. Chong, S. Pickering, and A. Boglietti, *Cooling of Rotating Electrical Machines* (Institute of Engineering and Technology, 2022).

28. Y. C. Chong, *Thermal Analysis and Air Flow Modelling of Electrical Machines* (University of Edinburgh, 2015).

29. Ansys CFX-Solver, Ansys CFX-Solver Modeling Guide (ANSYS, 2023).

30. A. Boglietti, A. Cavagnino, and D. Staton, "Determination of Critical Parameters in Electrical Machine Thermal Models," *IEEE Transactions on Industry Applications* 44, no. 4 (2008): 1150–1159, https://doi.org/10.1109/tia.2008.926233.

31. G. J. Li, Z. Q. Zhu, M. Foster, and D. Stone, "Comparative Studies of Modular and Unequal Tooth PM Machines Either With or Without Tooth Tips," *IEEE Transactions on Magnetics* 50, no. 7 (2014): 1–10, https://doi.org/10.1109/tmag.2014.2310179.

32. Y. C. Chong, D. A. Staton, M. Mueller, and J. Chick, "Pressure Loss Measurement in Rotor-Stator Gap of Radial Flux Electrical Machines," in *2014 International Conference on Electrical Machines (ICEM* (IEEE, 2014), 2172–2178.